Supplementary Information

Monitoring long-term cardiac activity with contactless radio frequency signals

Contents

1 Supplementary Note 1: Sensing Signals

1.1 RF signals

Our system is based on the radio frequency (RF) signals emitted by a Frequency Modulated Continuous-Wave (FMCW) radar, which has 3 transmitting antennas and 4 receiving antennas. The frequency of the transmitted signal increases linearly, with an initial frequency of f_c and a bandwidth of B. After receiving the echo signal, the radar mixes the received signal with the transmitted signal and then generates the intermediate frequency (IF) signal, which can be expressed as:

$$y(t) = A \cdot e^{-j \cdot 2\pi \cdot f_c \cdot \tau}, \tag{1}$$

where $\tau = \frac{2d}{c}$ denotes the delay of signal propagation, d represents the distance between an object and the radar, c is the signal propagation speed in the air, and A denotes the amplitude of the received signal.

The range resolution is related to the bandwidth of the transmitted signal and can be calculated as:

$$d_{res} = \frac{c}{2B}. \tag{2}$$

When we use a bandwidth of 4 GHz, we can achieve a range resolution of 3.75 cm. However, for measuring sub-centimeter scale movement like heartbeat, we need to capture the phase change of the millimeter-wave signals, whose relation with the movement is:

$$\Delta\phi = 2\pi \cdot \frac{2\Delta d}{c} = \frac{4\pi \cdot \Delta d}{c}, \tag{3}$$

where Δd denotes the related movement, and $\Delta\phi$ is the phase change caused by the movement.

1.2 Sensing model

When the transmitted signals hit the human chest, they will be modulated by the heartbeat micro-motion and respiratory micro-motion according to Equation 3. As a result, the reflected signals containing heartbeat and respiratory information can be represented as:

$$y(t) = A \cdot e^{-j \cdot 2\pi \cdot f_c \cdot (\Delta\tau_{cmov}(t) + \tau_{ini})}, \tag{4}$$

where τ_{ini} is the initial delay related to the distance between the individual and the radar. $\Delta\tau_{cmov}(t)$ denotes the delay caused by the chest movement consisting of both respiratory and heartbeat micro-motion. Therefore, our work aims to extract the heartbeat micro-motion from the mixed signals.

1.3 2D FFT

The details of the 2D FFT as follows:

Range FFT. The radar continuously transmits FMCW signals, also known as chirps. The radar's mixer combines the received chirp with the transmitted chirp to produce an IF signal. The relationship between the frequency change of the IF signal Δf and the distance d can be expressed as:

$$\Delta f = S \cdot \tau = \frac{S \cdot 2d}{c} \Rightarrow d = \frac{\Delta f \cdot c}{2S}, \tag{5}$$

where S represents the slope of the chirp, c is the speed of the signal, and d is the distance between the radar and the object. Thus, the range of the detected object can be obtained by performing a Fast Fourier Transform (FFT) for each chirp.

Angle FFT. The relationship between the phase difference $\Delta\phi$ and the Angle of Arrival (AoA) θ is described by:

$$\Delta\phi = \frac{2\pi l sin\theta}{\lambda}, \tag{6}$$

where l represents the distance between adjacent receiving antennas, and λ is the wavelength. Hence, by performing another FFT along chirps from different receiving antennas, we can obtain the AoA of the target.

2 Supplementary Note 2: Respiratory spectra leakage

The heart's electrical system generates rhythmic impulses that orchestrate the muscular contractions, resulting in the heartbeat. The normal heart rate for adults under normal conditions is approximately 60 to 100 beats per minute [1]. The mechanical activity of cardiac pulsation induces rhythmic subtle movements on the body surface. In addition, respiration induces periodic changes in chest movements. The typical respiratory rate for a healthy individual is approximately 12 to 20 periods per minute [2]. Existing methods [3–5] utilized frequency differences between the two micro-motions to separate them. However, the obtained heartbeat information suffers from poor signal to interference plus noise ratio (SINR) due to respiratory spectra leakage. This is because the frequencies of the two micro-motions are relatively close, and the quasi-periodic respiration will generate higher-frequency harmonics, causing interference in the heartbeat frequency range. Additionally, due to the significantly greater magnitude of respiration compared to heartbeats, this interference is even more pronounced.

In order to provide a more comprehensive understanding of this phenomenon, we conducted a series of comparative experiments. We utilized a millimeter-wave radar to capture chest reflection signals in the proximity of the heart. This was done for individuals in both a normal breathing state and during breath-holding. Figure 1a displays the frequency-domain distribution of the received signals from an individual in a breath-holding state. The presence of the heartbeat frequency is evident, enabling the extraction of a clean heartbeat pattern. Consequently, the estimation of heartbeats exhibits excellent performance, as depicted in Figure 1b. However, when analyzing signals from individuals with normal breathing, a notable interference arises. This interference stems from respiratory harmonics that significantly contaminate the frequency range associated with heartbeat signals, as illustrated in Figure 1c. Consequently, the estimation of heartbeats encounters a considerable decline in performance, as demonstrated in Figure 1d. These findings demonstrate the significant interference caused by respiratory spectrum leakage in heartbeat estimation. Therefore, suppressing such interference is essential to improve the system performance.

3 Supplementary Note 3: Understanding heartbeat

The heartbeat signals are quasi-periodic due to the periodic cardiac mechanical movement. Therefore, the heartbeat signal can be regarded as a fundamental frequency signal whose frequency is equal to the heartbeat frequency and its harmonics. To support this argument, we collected data from a subject during breath holding and then transformed the received signal into the frequency domain. The frequency distributions of the reflected signal is depicted in Figure 2a. It is apparent that the heartbeat signal consists of a fundamental frequency signal and multiple harmonics. These harmonics have frequencies that are integer multiples of the heartbeat frequency. To gain further insight, we collected signals reflected from a subject engaged in normal breathing and transformed them into the frequency domain. From Figure 2b, it can be observed that despite the interference caused by respiratory harmonics, the presence of heartbeat harmonics can still be distinguished. Notably, due to the lower frequency of respiration, its harmonics primarily concentrate in the relatively low-frequency range. As the frequency increases, the respiratory harmonics rapidly diminish, leading to the dominance of heartbeat harmonics in the high-frequency band.

In addition to the frequency analysis, we further evaluated the signal-to-interference-plus-noise ratio (SINR) of the heartbeat harmonics across different frequency bands. Figure 2c demonstrates the SINR trend. We can observe that as the frequency increases, the SINR of the heartbeat harmonics gradually increases, reaching its maximum at the 14-16 Hz range. However, beyond 16 Hz, the SINR of the heartbeat harmonics starts to decrease. This decline can be attributed to the relatively lower energy of the heartbeat harmonics and the increasing influence of noise. Given these findings, we ask this question: Can we leverage the high-frequency component of the received signal to extract clean heartbeat patterns?

4 Supplementary Note 4: Beat frequency effect

4.1 Principle of the beat frequency effect

The beat frequency effect refers to that when two waves of different frequencies interact with each other, they will produce a periodic pattern due to constructive and destructive interference. The frequency of the pattern is related to the frequency difference of the two waves. To elucidate this principle, we assume that there are two waves $x_1(t)$ and $x_2(t)$ with the same direction but different frequencies, which can be expressed by:

$$x_1(t) = A \cdot cos(2\pi f_1 t + \varphi), \tag{7}$$
$$x_2(t) = A \cdot cos(2\pi f_2 t + \varphi), \tag{8}$$

where A represents the amplitude of the two waves, f_1 and f_2 denote the frequency of the two waves, respectively, and φ is the initial phase of the two waves. Hence, the combined wave $x(t)$ can be represented as:

$$\begin{aligned} x(t) &= x_1(t) + x_2(t) &(9)\\ &= A \cdot cos(2\pi f_1 t + \varphi) + A \cdot cos(2\pi f_2 t + \varphi) &(10)\\ &= A \cdot cos 2\pi \frac{f_1 - f_2}{2} t \cdot cos(2\pi \frac{f_1 + f_2}{2} t + \varphi). &(11) \end{aligned}$$

According to the sum and difference formulas of trigonometric functions, this combined wave can be represented by the dot product of the two new cosine waves (Eq. 9), where the frequencies of the two new cosine waves are $\frac{f_1 - f_2}{2}$ and $\frac{f_1 + f_2}{2}$, respectively. Since $\frac{f_1 - f_2}{2}$ is relatively small, $A \cdot cos 2\pi \frac{f_1 - f_2}{2} t$ changes slowly over a longer period, forming a periodic modulating pattern known as "beat frequency pattern", which is called beat frequency effect (Fig. 3a).

Furthermore, Figure 3a shows that a beat frequency period consists of the two heartbeat patterns, which results in the frequency of heartbeat patterns of $f_1 - f_2$. To validate the principle, we simulated two signals with frequencies of 6 Hz and 7 Hz, then combined them. From Figure 3b, we observed a pattern with a frequency of 1 Hz, which showcases the presence of the beat frequency effect.

4.2 Beat frequency effect in heartbeat

An interesting discovery is the occurrence of the beat frequency effect among the heartbeat harmonics, resulting in beat frequency patterns. For example, $h_{i-1}(t)$ and $h_i(t)$ represent two adjacent harmonics of the heartbeat. When combined, they create a beat frequency effect, generating the beat frequency patterns as follows:

$$\begin{aligned} &h_i(t) + h_{i-1}(t) &(12)\\ &= A \cdot cos(2\pi f_i t + \varphi) + A \cdot cos(2\pi f_{i-1} t + \varphi) &(13)\\ &= A \cdot cos 2\pi \frac{f_i - f_{i-1}}{2} t \cdot cos 2\pi (\frac{f_i + f_{i-1}}{2} t + \varphi) &(14)\\ &= A \cdot cos \frac{f}{2} t \cdot cos 2\pi (\frac{f_i + f_{i-1}}{2} t + \varphi) &(15) \end{aligned}$$

where f denotes the frequency of the heartbeat. From Eq. 12, we can see that the two harmonics of the heartbeat $h_{i-1}(t)$ and $h_i(t)$ generate the beat frequency patterns with a frequency of $\dfrac{f_i - f_{i-1}}{2}$. Furthermore, as each beat frequency period contains two heartbeat patterns, the frequency of the heartbeat patterns is denoted by $f_i - f_{i-1}$. Given that $f_i - f_{i-1} = f$, the occurrence frequency of the heartbeat patterns is f.

In such a way, we can estimate the heartbeat information by utilizing the beat frequency effect in the heartbeat harmonics. To show this, we conducted experiments on subjects with breath-holding (Fig. 3c) and normal breathing (Fig. 3d), respectively. We extracted the high-frequency component from the signals, which contain the high-order harmonics of the heartbeat. Figure 3c,d display the distinct heartbeat patterns due to the beat frequency effect of the high-order harmonics.

5 Supplementary Note 5: System design

5.1 Signal selection.

In previous studies, various signal selection algorithms have been proposed to address the challenge of extracting accurate and reliable signals, such as mmHRV [3], Mtrack [6], and BNR [7]. However, these algorithms have shown limitations in achieving satisfactory performance. The mmHRV algorithm utilizes self-correlation to identify the signal with the strongest correlation to other signals. Mtrack employs a differential accumulation approach in the time domain. It selects the voxel point with the highest differential cumulative energy. BNR, as its name suggests, is based on the Breathing-to-Noise Ratio. This method aims to identify the signal with the maximum breath signal-to-noise ratio.

However, due to the different positions of the heartbeats and breaths within the chest cavity, the maximal breath signal-to-noise ratio cannot guarantee abundant heartbeat information. Therefore, in this paper, we propose a signal selection algorithm to identify the signal with the rich heartbeat information from various signals reflected by the chest. This method is based on the observation that for the same individual, a signal with richer heartbeat information experiences less interference, leading to a more stable estimation of IBIs. Specifically, we first utilize each signal $S(t)$ reflected from different chest voxels to estimate the IBI. Then, we calculate the variance of each IBI sequence individually as follows

$$\mathrm{var}^{(\mathrm{j})} = \frac{1}{\mathrm{N}_{\mathrm{IBI}^{(\mathrm{j})}}} \sum_{\mathrm{i}=1}^{\mathrm{N}_{\mathrm{IBI}^{(\mathrm{j})}}} (\mathrm{IBI}_{\mathrm{i}}^{(\mathrm{j})} - \overline{\mathrm{IBI}^{(\mathrm{j})}})^2, \tag{16}$$

where $\mathrm{var}^{(\mathrm{j})}$ denotes the variance of j-th IBIs sequence $\mathrm{IBI}^{(\mathrm{j})}$ that estimated from signal $S^{(i)}(t)$. Finally, we adopt the signal with the smallest variance of IBIs as the optimal signal.

5.2 VMD

To extract the heartbeat patterns from the received RF signals, we employ the Variational Mode Decomposition (VMD) algorithm [8] to decompose the input signals into different frequency components. The goal of VMD is to decompose a real-valued input signal into a discrete number of sub-signals or modes, denoted as u_k. These modes possess specific sparsity properties while accurately representing the input signal. Each mode k is predominantly concentrated around a central pulsation ω_k. The decomposition process involves solving a constrained variational problem. The specific formulation of this problem is as follows:

$$\min_{\{u_k\},\{\omega_k\}} \left\{ \sum_k \left\| \partial_t [(\delta(t) + \frac{j}{\pi t}) * u_k(t)] e^{-j\omega_k(t)} \right\|_2^2 \right\} \tag{17}$$

$$s.t. \quad \sum_k u_k = f \tag{18}$$

Then, the augmented Lagrangian is introduced as follows

$$L(\{u_k\}, \{\omega_k\}, \lambda) = \alpha \sum_k \left\| \partial_t[(\delta(t) + \frac{j}{\pi t}) * u_k(t)]e^{-j\omega_k(t)} \right\|_2^2 + \left\| f(t) - \sum_k u_k(t) \right\|_2^2 \tag{19}$$

$$+ \left\langle \lambda(t), f(t) - \sum_k u_k(t) \right\rangle . \tag{20}$$

The solution is the alternate direction method of multipliers (ADMM) [9, 10]. The complete process of VMD is summarized in algorithm 1.

Compared to other methods such as band-pass filtering and second-order difference, one key advantage of VMD is that it can adaptively divide the frequency band of the signal based on the frequency distribution, enabling the extraction of high-frequency components that contain rich heartbeat information. In this work, the number of components in the VMD algorithm is experimentally set to 5. As shown in Figure 4, after decomposing the raw signal using VMD, five components, labeled as Imf 1 to Imf 5, are obtained. These components span a range of frequencies from low to high. Specifically, Imf 1 represents the direct current component, Imf 2 corresponds to the respiratory component, and Imf 3 captures the heartbeat component within the frequency band associated with heartbeats. However, the presence of respiratory spectrum leakage in Imf 3 affects the quality of the extracted heartbeat information. Imf 5, the highest frequency component obtained through VMD, contains relatively pristine heartbeat information as it is located farther away from respiratory interference. To visualize the frequency distribution of Imf 5, a Fast Fourier Transform (FFT) transformation is performed on it. Figure 4 demonstrates that Imf 5 primarily consists of high-order harmonics of the heartbeat, indicating the presence of clear and distinct heartbeat information within this component.

6 Supplementary Note 6: Evaluation metric of Real-Time IBI

In this paper, we employ a metric called Real-time IBI (RT-IBI) to evaluate the performance of the system in monitoring heart rate variability (HRV). Once obtained the heartbeat patterns, we utilize a peak-finding algorithm to identify the moments corresponding to each peak value. By calculating the time difference between consecutive heartbeat moments, we can obtain a sequence of Inter-Beat Intervals (IBIs).

To provide a comprehensive evaluation of the system's performance, we further process the IBIs into a real-time IBI representation, which is visualized as a 2-dimensional line chart, as depicted in Figure 5. This line chart consists of multiple line segments, where each segment corresponds to an individual IBI in the sequence. The length of each segment represents the duration of the IBI, while its height indicates the magnitude of the IBI value.

To generate the line chart, we create line segments of varying lengths based on the magnitude of each IBI in the sequence. These line segments are then connected end-to-end, forming a continuous line chart. The vertical position of each segment corresponds to the magnitude of its respective IBI. Each point on the line segments has a horizontal coordinate representing a specific moment in time, and a vertical coordinate representing the IBI value at that moment.

Using RT-IBI as a metric for evaluating the system's performance offers two significant advantages. Firstly, RT-IBI provides a more realistic and comprehensive assessment compared to using IBI alone. Figure 6 demonstrates that when the heartbeat pattern of the RF signal is lost due to interference, the intervals between consecutive heartbeats increase. This results in longer line segments with higher positions in the RT-IBI representation, leading to larger RT-IBI errors (e.g., 21.2 ms). By accurately reflecting the system's ability to extract heartbeat information, RT-IBI provides a more accurate evaluation of performance. In contrast, using IBI alone for performance estimation can lead to an overestimation of the system's capabilities. When the heartbeat pattern is disrupted, it becomes challenging to match the length of the estimated IBI sequence with the ground truth IBI sequence. Previous methods addressed this issue by discarding periods of time where the heartbeat estimation and ground truth patterns do not occur simultaneously. IBI errors were then calculated based on the remaining time periods. However, this approach resulted in an underestimation of the IBI error (e.g., 8.4 ms) compared to the actual error.

Secondly, RT-IBI provides a value corresponding to each moment in time, offering an intuitive display of the IBI at any given time. Figure 6 illustrates this aspect, where the RT-IBI representation clearly shows the variations in IBI values over time. This visual depiction enhances the understanding and analysis of the temporal dynamics of heart rate variability.

7 Supplementary Figure 1: Respiratory spectra leakage.

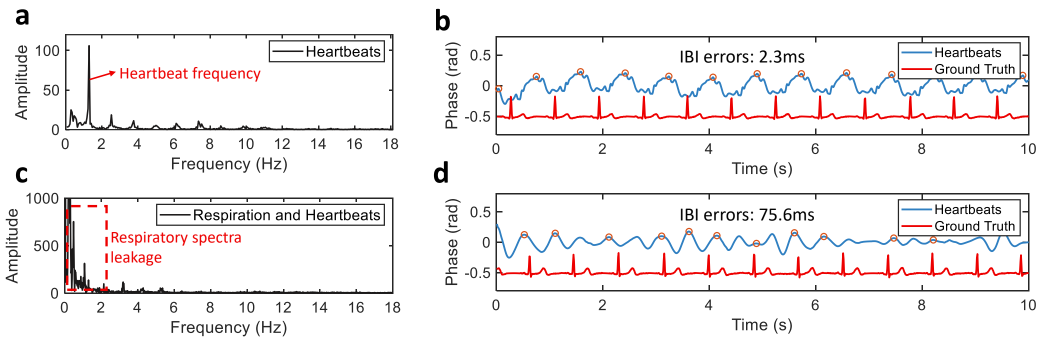

Figure 1: **Respiration spectra leakage.** Due to the close frequencies of respiratory and heartbeat signals, the respiratory harmonics would leak into the heartbeat band. Also, the strength of the respiratory signal is much stronger than that of the heartbeat. Consequently, the heartbeat information within the heartbeat band range has a low SINR. **a**, The frequency-domain distribution of the received signal during the breath-holding state, where the heartbeat frequency is clearly discernible. **b**, In this clean and distinct heartbeat pattern, the estimation performance of HRV is outstanding, with an IBI error as low as 2.3 ms. **c**, The frequency-domain distribution of the received signal during normal breathing. It is evident that the heartbeat frequency becomes contaminated by stronger respiratory harmonics. **d**, As a result, the presence of these respiratory harmonics significantly deteriorates the estimation performance of IBI.

8 Supplementary Figure 2: Effects of heartbeat harmonics.

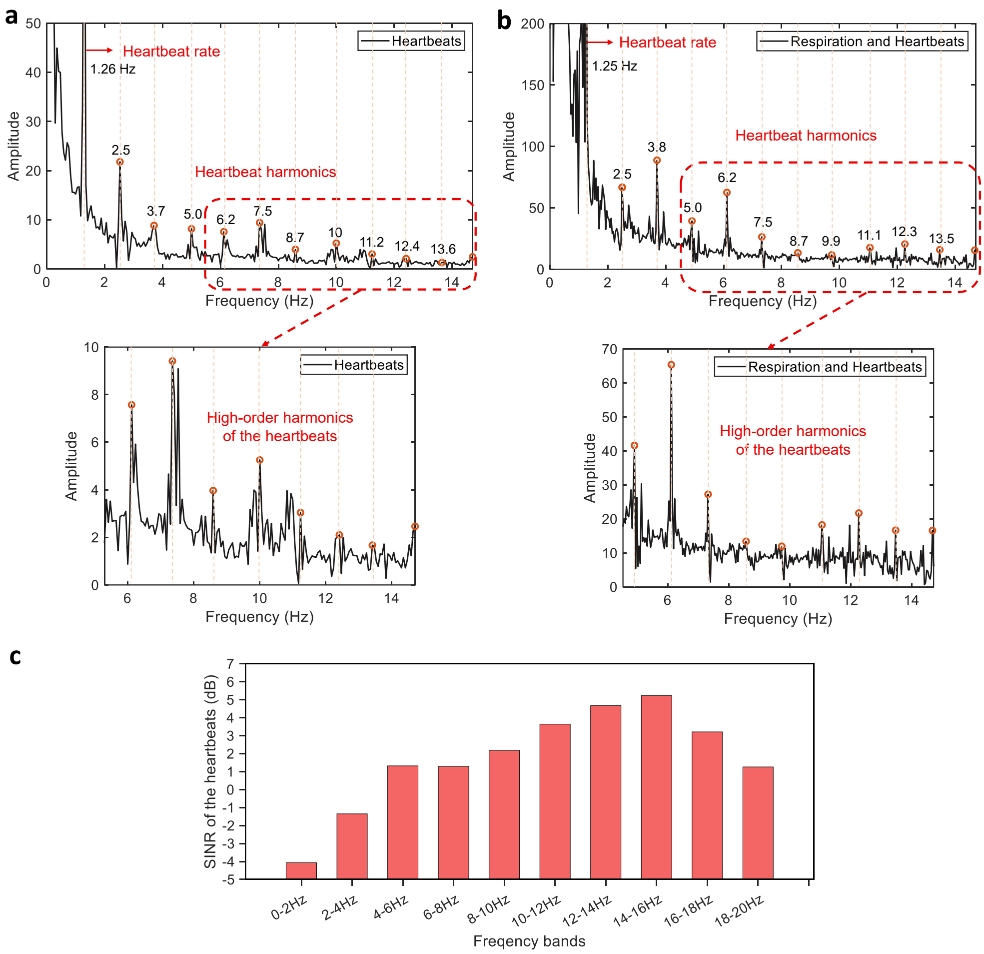

Figure 2: **Effects of heartbeat harmonics.** **a**, The frequency distribution of the received signal during breath-holding. The heartbeat signals can be considered as composed of a fundamental frequency signal and its harmonics. Moreover, in the high-frequency band, distinct evenly spaced frequencies can be observed, representing the high-order harmonics of the heartbeat. **b**, The frequency distribution of the received signal during normal breathing. While the harmonics of the heartbeat are contaminated by respiratory harmonics, they can still be recognized. Similarly to the breath-holding case, there are distinct evenly spaced frequencies in the high-frequency band, corresponding to the high-order harmonics of the heartbeat. **c**, The SINR of heartbeat harmonics in different frequency bands. As the frequency increases, the SINR of the heartbeat harmonics becomes higher. The frequency band of 14-16 Hz exhibits the maximum SINR.

9 Supplementary Figure 3: Beat frequency effect.

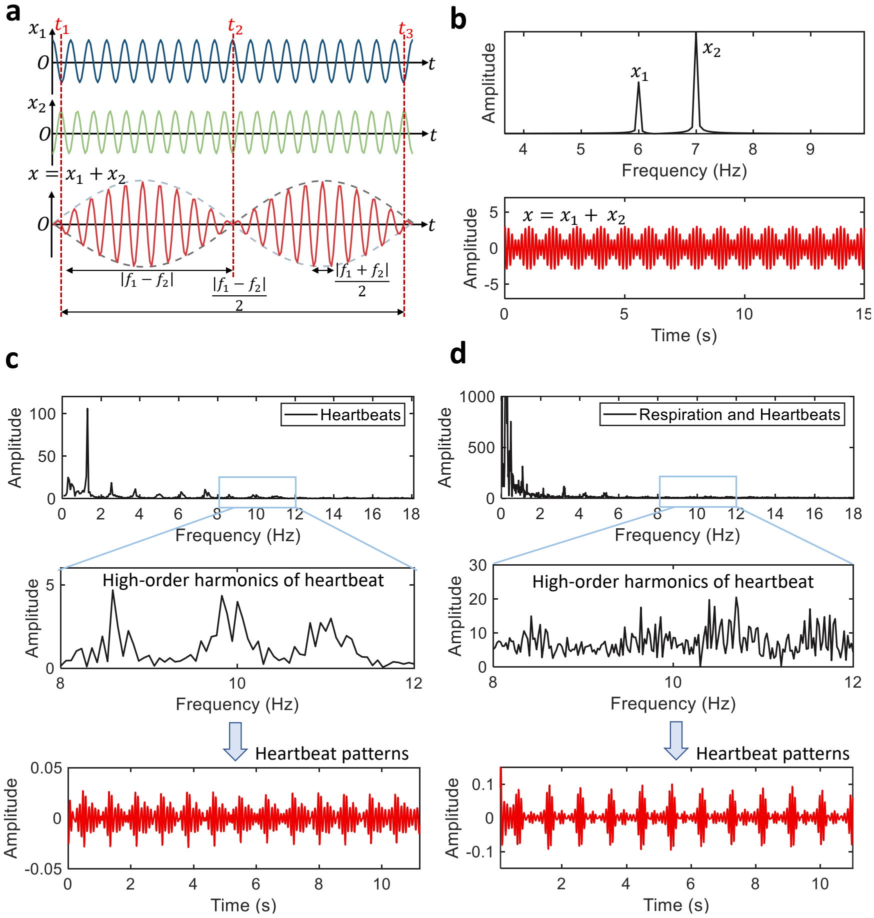

Figure 3: **Beat frequency effect.** **a**, The principle diagram of the beat frequency effect. When two waves with frequencies f_1 and f_2 are combined, a periodic variation with a frequency of $\frac{f_1 - f_2}{2}$ is generated. This periodic variation contains patterns with a frequency of $f_1 - f_2$. **b**, We simulated two waves with frequencies of 6 Hz and 7 Hz, and then combined them. As a result, we observed a pattern with a frequency of 1 Hz, which demonstrates the presence of the beat frequency effect. **c,d**, To further illustrate the impact of the beat frequency effect on the received signals, we isolated the high-frequency band from the received signals during both normal breathing and breath-holding, respectively. These isolated signals reveal the distinct heartbeat patterns resulting from the beat frequency effect.

10 Supplementary Algorithm 1: Complete optimization of VMD

Algorithm 1 Complete optimization of VMD

Initialize $\{\hat{u}_k^1\}, \{\omega_k^1\}, \hat{\lambda}^1, n \leftarrow 0$

repeat

set $n \leftarrow n+1$

for $k = 1 : K$ **do**

Update $\hat{u}_k$ for all $\omega \geq 0$:

$$\hat{u}_k^{n+1}(\omega) \leftarrow \frac{\hat{f}(\omega) - \sum_{i<k} \hat{u}_i^(n+1)(\omega) - \sum_{i>k} \hat{u}_i^n(\omega) + \frac{\lambda^n\hat{(}\omega)}{2}}{1 + 2\alpha(\omega - \omega_k^n)^2}$$

Update ω_k:

$$\omega_k^{n+1} \leftarrow \frac{\int_0^\infty \omega \left|\hat{u}_k^{n+1}(\omega)\right|^2 d\omega}{\int_0^\infty \left|\hat{u}_k^{n+1}(\omega)\right|^2 d\omega}$$

end for

Dual ascent for all $\omega \geq 0$:

$\hat{\lambda}^{n+1}(\omega) \leftarrow \hat{\lambda}^n(\omega) + \tau(\hat{f}(\omega) - \sum_k \hat{u}_k^{n+1}(\omega))$

until convergence: $\sum_k \left\|\hat{u}_k^{n+1} - \hat{u}_k^n\right\|_2^2 / \|\hat{u}_k^n\|_2^2 < \epsilon$.

11 Supplementary Figure 4: VMD signal decomposition process

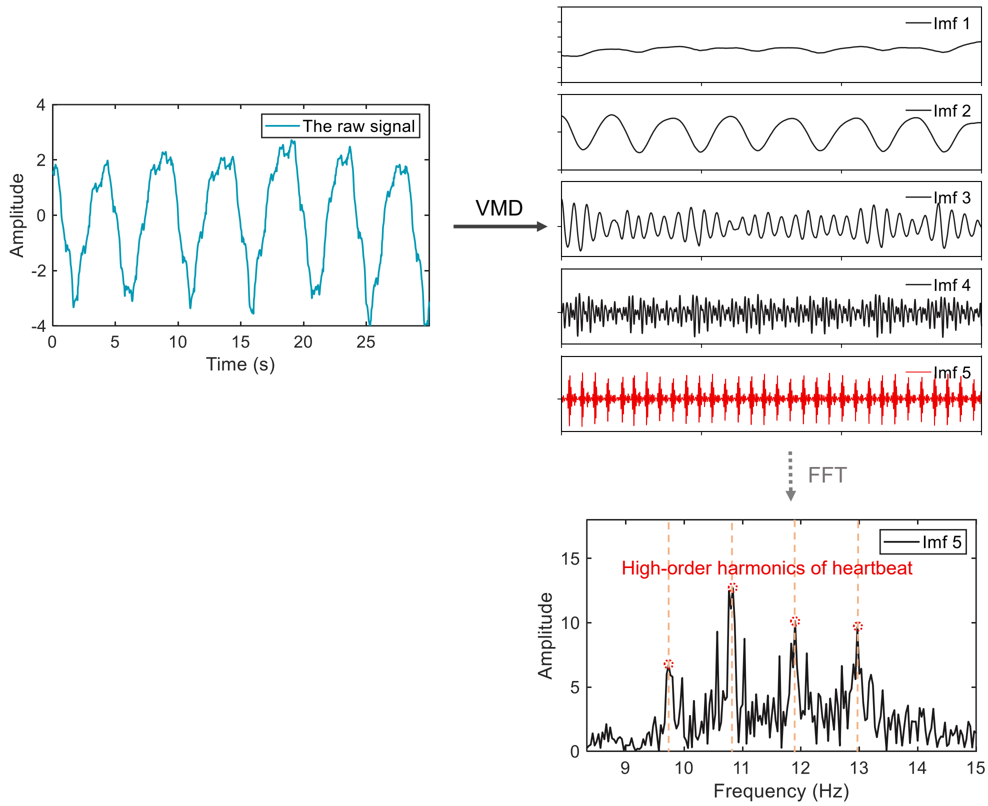

Figure 4: **VMD signal decomposition process.** In our approach, we employ the Variational Mode Decomposition (VMD) algorithm to decompose the RF signal into five different frequency components. Among these components, we specifically select the highest frequency component, Imf 5, to extract the heartbeat patterns. Furthermore, by examining the frequency domain plot of Imf 5, we can observe that this high-frequency component predominantly consists of the high-order harmonics of the heartbeat.

12 Supplementary Figure 5: Real-time IBI

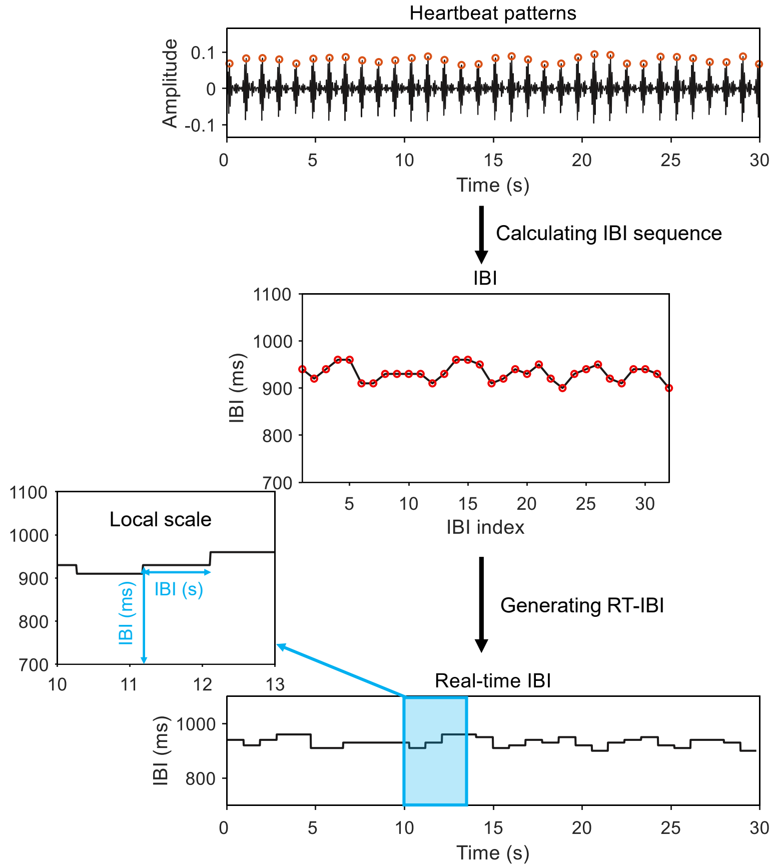

Figure 5: **Real-time interbeat interval (RT-IBI).** To obtain an IBI sequence, we calculate the difference between the moments when consecutive heartbeats occur. This IBI sequence serves as the basis for generating a 2-dimensional line chart called RT-IBI. In the RT-IBI chart, the entire line is formed by connecting multiple line segments, with each segment corresponding to one IBI in the IBI sequence. The length of each segment represents the duration of that particular IBI, while the height indicates the magnitude of the IBI value. Each point on the line segments has a horizontal coordinate representing a specific moment in time and a vertical coordinate representing the corresponding IBI value at that moment.

13 Supplementary Figure 6: Comparison between Real-time IBI and IBI

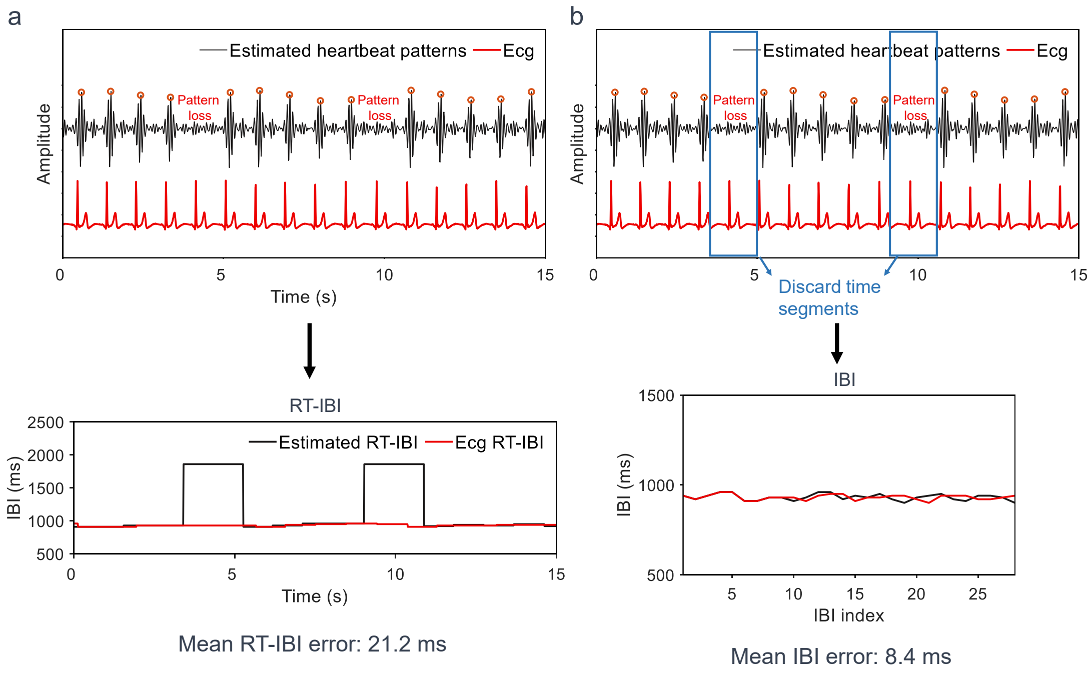

Figure 6: **Comparison between Real-time IBI and IBI.** When the received RF signal is disturbed, it can result in anomalies in the extracted heartbeat pattern, such as loss or redundancy. In such cases, utilizing the RT-IBI chart to assess the system's performance provides a more realistic and comprehensive evaluation compared to using only the IBI. **a**, When the heartbeat pattern in the RF signal is lost, the intervals between two adjacent heartbeats will increase. This leads to the corresponding line segments being longer and positioned higher, resulting in a larger RT-IBI error. In such a way, RT-IBI can accurately reflect the system's ability to extract heartbeat information. **b**, In contrast, previous methods that utilized only the IBI for estimating system performance could lead to an overestimation of the system's capabilities. For instance, when the heartbeat pattern is lost, the length of the estimated IBI sequence may not match the length of the ground truth IBI sequence. Consequently, it becomes impossible to calculate the IBI error accurately. To handle this issue, previous methods often discarded periods where the heartbeat estimation pattern and the ground truth pattern did not occur simultaneously. Then, they calculated the IBI error based on the remaining periods. However, this approach resulted in an underestimation of the estimation error compared to the actual error experienced in the system.

14 Supplementary Figure 7: Comparison to standard measurement

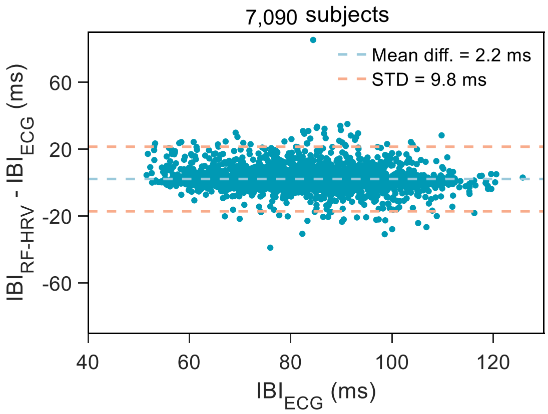

Figure 7: **Real-time IBI data collected in large-scale clinical scenarios and comparison to standard measurement.** Bland-Altman plots comparing real-time IBI determined using the RF-HRV system with ECG device (7,090 subjects).

15 Supplementary Figure 8: Multiple examples of the heartbeat patterns

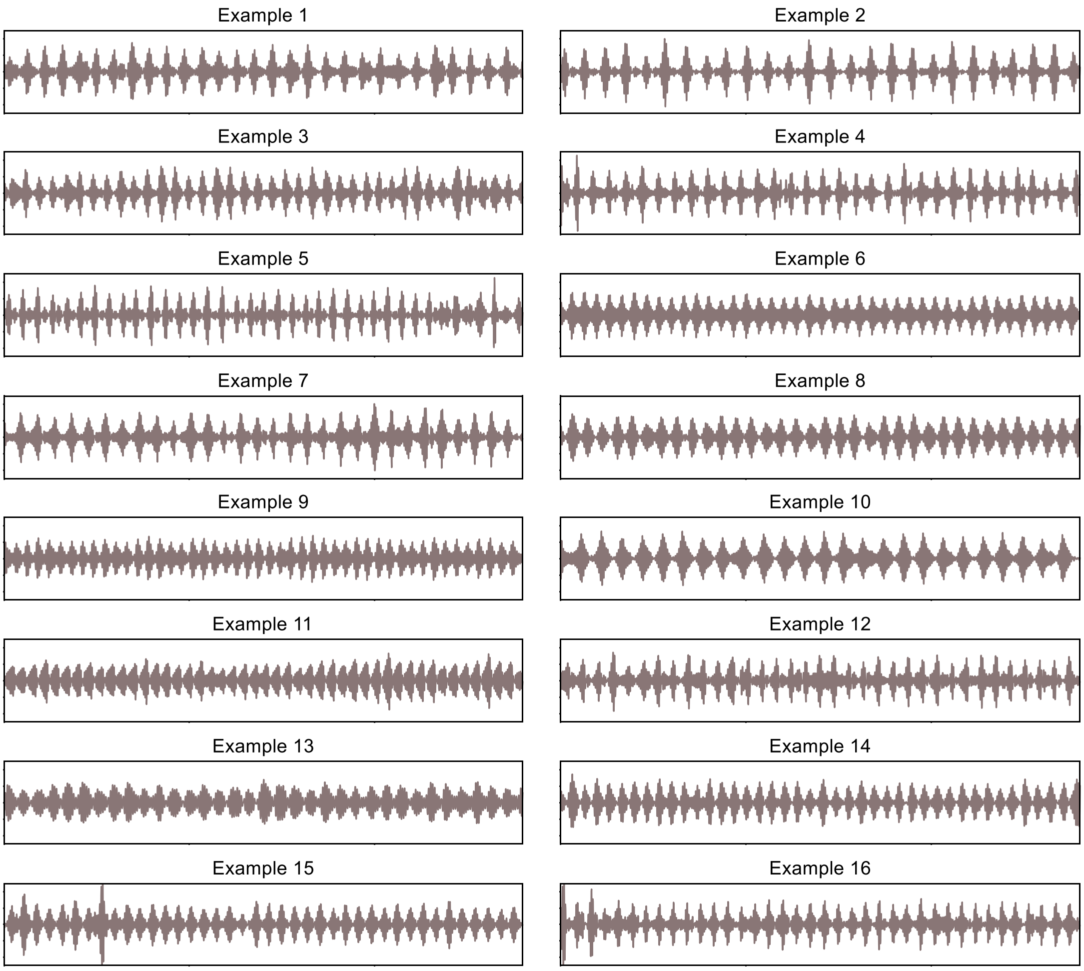

Figure 8: **Multiple examples of heartbeat patterns resulting from beat frequency effect.**

References

[1] R. Acharya U, K. N, O. W. Sing, L. Y. Ping, and T. Chua, "Heart rate analysis in normal subjects of various age groups," *Biomedical engineering online*, vol. 3, pp. 1–8, 2004.

[2] P. H. Charlton, D. A. Birrenkott, T. Bonnici, M. A. Pimentel, A. E. Johnson, J. Alastruey, L. Tarassenko, P. J. Watkinson, R. Beale, and D. A. Clifton, "Breathing rate estimation from the electrocardiogram and photoplethysmogram: A review," *IEEE reviews in biomedical engineering*, vol. 11, pp. 2–20, 2017.

[3] F. Wang, X. Zeng, C. Wu, B. Wang, and K. R. Liu, "mmhrv: Contactless heart rate variability monitoring using millimeter-wave radio," *IEEE Internet of Things Journal*, vol. 8, no. 22, pp. 16 623–16 636, 2021.

[4] T. Zheng, Z. Chen, C. Cai, J. Luo, and X. Zhang, "V2ifi: In-vehicle vital sign monitoring via compact rf sensing," in *Proc. ACM Interact. Mob. Wearable Ubiquitous Technol*, 2020.

[5] F. Adib, H. Mao, Z. Kabelac, D. Katabi, and R. C. Miller, "Smart homes that monitor breathing and heart rate," in *Proceedings of the 33rd annual ACM conference on human factors in computing systems*, 2015, pp. 837–846.

[6] D. Zhang, Y. Hu, and Y. Chen, "Mtrack: Tracking multiperson moving trajectories and vital signs with radio signals," *IEEE Internet of Things Journal*, vol. 8, no. 5, pp. 3904–3914, 2020.

[7] S. Yue, H. He, H. Wang, H. Rahul, and D. Katabi, "Extracting multi-person respiration from entangled rf signals," *Proceedings of the ACM on Interactive, Mobile, Wearable and Ubiquitous Technologies*, vol. 2, no. 2, pp. 1–22, 2018.

[8] K. Dragomiretskiy and D. Zosso, "Variational mode decomposition," *IEEE transactions on signal processing*, vol. 62, no. 3, pp. 531–544, 2013.

[9] M. R. Hestenes, "Multiplier and gradient methods," *Journal of optimization theory and applications*, vol. 4, no. 5, pp. 303–320, 1969.

[10] D. P. Bertsekas, *Constrained optimization and Lagrange multiplier methods.* Academic press, 2014.